Research Article | Vol. 14, No. 11 / 1 Nov 2023 / Biomedical Optics Express 5642
Biomedical Optics EXPRESS

# Tracking the dynamics of thrombus formation in a blood vessel-on-chip with visible-light optical coherence tomography

CARLOS CUARTAS-VÉLEZ,[1,†,*] HELEEN H. T. MIDDELKAMP,[2,4,†] ANDRIES D. VAN DER MEER,[3] ALBERT VAN DEN BERG,[2] AND NIENKE BOSSCHAART[1]

[1]*Biomedical Photonic Imaging Group, Faculty of Science and Technology, University of Twente, Enschede, The Netherlands*
[2]*BIOS/Lab on a Chip, Faculty of Electrical Engineering, Mathematics and Computer Science, University of Twente, Enschede, The Netherlands*
[3]*Applied Stem Cell Technologies, Faculty of Science and Technology, University of Twente, Enschede, The Netherlands*
[4]*h.h.t.middelkamp@utwente.nl*
[†]These authors contributed equally to this work.
[*]*c.a.cuartasvelez@utwente.nl*

**Abstract:** Thrombus formation is a physiological response to damage in a blood vessel that relies on a complex interplay of platelets, coagulation factors, immune cells, and the vessel wall. The dynamics of thrombus formation are essential for a deeper understanding of many disease processes, like bleeding, wound healing, and thrombosis. However, monitoring thrombus formation is challenging due to the limited imaging options available to analyze flowing blood. In this work, we use a visible-light optical coherence tomography (vis-OCT) system to monitor the dynamic process of the formation of thrombi in a microfluidic blood vessel-on-chip (VoC) device. Inside the VoC, thrombi form in a channel lined with a monolayer of endothelial cells and perfused by human whole blood. We show that the correlation of the vis-OCT signal can be utilized as a marker for thrombus formation. By thresholding the correlation during thrombus formation, we track and quantify the growth of the thrombi over time. We validate our results with fluorescence microscopic imaging of fibrin and platelet markers at the end of the blood perfusion assay. In conclusion, we demonstrate that the correlation of the vis-OCT signal can be used to visualize both the spatial and temporal behavior of the thrombus formation in flowing human whole blood.



## 1. Introduction

Thrombus formation is a physiological response to prevent excessive blood loss when a blood vessel is damaged. When a vascular injury occurs, platelets become activated and interact with the extracellular matrix underneath the vascular endothelium, causing them to adhere to the injured vessel. The activated platelets form a stable plug held in place with fibrin. Under hemostatic circumstances, thrombi are dissolved during fibrinolysis and cleared by the body [1,2]. However, coagulation disorders, endothelial dysfunction, and hyperinflammation can affect the normal formation or clearing of a thrombus, thus increasing the risk for severe health-threatening diseases such as deep vein thrombosis [3,4], pulmonary embolism [5], stroke [6,7], and heart attack [8,9]. Consequently, understanding, parameterizing, and measuring the formation of thrombi is essential for developing preventive and therapeutic strategies for many cardiovascular and hematologic disorders.

#500434 https://doi.org/10.1364/BOE.500434
Journal © 2023 Received 14 Jul 2023; revised 31 Aug 2023; accepted 3 Sep 2023; published 9 Oct 2023

Biomedical Optics EXPRESS

Several techniques focusing on different physical properties of blood have emerged to monitor thrombus formation [10]. These techniques include electrical [11–13] and electrochemical [14] signals, electro-mechanical analysis [15–17], photoacoustics (PA) [18,19] and optical coherence tomography (OCT) [20–22]. Although most methods provide precise assessments, one of their main limitations lies in requiring a static state or non-physiological flow of the blood. Therefore, they lack applicability to detailed studies of thrombus formation, where the shear wave velocity, vessel size, and hematocrit modify the clotting process [20,23]. Due to their non-invasive and imaging capabilities, PA- and OCT-based methods that can analyze flowing blood have become attractive approaches.

In PA, an acoustic transducer detects acoustic waves produced by the tissue after excitation with a pulsed laser. In the case of forming thrombi, the changes in absorption are detectable in the PA signal, revealing its composition and age [18,19]. However, PA application remains restricted due to limited spatial and temporal resolution and high background noise. Moreover, monitoring blood clotting with OCT is growing in attention due to its potential application *in vivo* and capability to characterize properties of whole blood non-invasively, such as hematocrit [24], blood oxygen saturation [25], blood fibrinogen level [26], and total hemoglobin concentrations [27]. OCT uses backscattered light to create high-resolution images of tissue [28]. In the case of blood, the changes in viscoelastic properties during thrombus formation directly influence the absorption and scattering experienced by light [22,23]. Therefore, monitoring the dynamics of thrombi formation based on the OCT signal over time has been demonstrated.

By evaluating the decay of the OCT signal in clotting blood, Xu et al. have investigated the clotting time under static and dynamic conditions for different blood flow velocities, hematocrits, tube sizes, and fibrinogen levels [20,23,26]. Furthermore, the authors developed an optical coherence elastography (OCE) method to obtain viscoelastic properties of blood by estimating shear wave velocities and mechanical displacements [21]. However, OCE requires specialized equipment to induce mechanical waves with quantifiable movements. More recently, Tang et al. proposed a correlation-based technique to determine the coagulation time, thrombus formation duration, and thrombus strength from the autocorrelation of the OCT signal at different clotting stages [22]. However, these works have characterized blood coagulation by analyzing the behavior of consecutive A-lines of flowing blood through capillary glasses, thus imaging forming thrombi inside the blood flow has not been achieved. The difficulty in imaging and quantifying thrombus formation arises from the challenging differentiation and localization of developing thrombi in free-flowing blood based on the OCT signal. This limitation is magnified due to a lack of adherence of the thrombi to the capillary glass, thus forming thrombi being flushed from the imaging area. We aim to overcome those limitations by combining spatial and temporal analysis of the correlation of the OCT signal while imaging thrombi formation in clotting blood. The blood flows through a vessel-on-chip (VoC) device that provides a human blood vessel model with cellular-level interaction between blood and endothelial cells.

VoC devices are micro-physiological systems designed to mimic human vessels by culturing human vascular cells in a spatially controlled, dynamically perfused microenvironment. [29–36]. VoC models are used for studying vascular inflammation and employ blood perfusion assays to unveil the underlying mechanisms of these processes [37–45], thus thrombus formation has been previously simulated [46–48]. The dynamics of the formation of a thrombus rely on the interplay of many parameters, such as platelet behavior [49,50]. Real-time information about the dynamic formation of a thrombus can facilitate understanding thromboembolic events that occur under different types of flow, thus easing anti-thrombotic drug development [51–53]. Using fluorescence microscopy, VoCs can reveal the aggregation of thrombus components, such as platelets and fibrin, during and after active blood perfusion. However, fluorescence microscopy is a limited read-out, as it relies on selected markers. Furthermore, these techniques only provide insight into two-dimensional end-point read-outs. Therefore, three-dimensional, non-invasive, and real-time

Biomedical Optics EXPRESS

monitoring methods such as OCT present an opportunity to understand the dynamics of thrombus formation in these VoC devices [54,55].

In this work, we combine OCT with a microfluidic VoC device to monitor thrombus formation in real time inside flowing blood. The VoC device mimics the interaction between endothelial cells and human whole blood, thus allowing the localization of thrombi. Thrombi formation inside the VoC is imaged with a visible-light OCT (vis-OCT) system during a blood perfusion assay. We develop a method to monitor the progression of the thrombi based on the correlation of the OCT signal. The correlation analysis can follow the development of thrombi throughout the duration of the perfusion assay, and the differences in the correlation indicate the formation and growth of thrombi inside the blood flow. We validate our results with microscopy images of labeled fibrin and platelets after the blood perfusion assay. This OCT thrombus formation technique can be used to observe thrombus formation on other VoC devices, where multidimensional thrombus formation observations can lead to a better understanding of clotting disorders and other vascular diseases.

## 2. Materials and methods

### *2.1. Microfluidic vessel-on-chip device*

#### 2.1.1. Microfluidic chip fabrication

The microfluidic chip consists of 4 channels which are 1 cm in length and $300 \times 52$ μm in width and height (as shown in Fig. 1(a) and Fig. 1(b)). The chip was fabricated by polydimethylsiloxane (PDMS, Sylgard 184, Mavom, the Netherlands)-based soft lithography using a wafer, which was produced by SU-8-based lithography using designs made in CleWin (WieWin software, the Netherlands) [34,37]. PDMS was added to the wafer at a ratio of 10 : 1 (base: crosslinker), left to cure overnight at 65°C, and removed after. Inlet and outlet holes of 1 mm were created employing biopsy punchers (RBP-10P, Robbins Instruments, USA). PDMS was spin-coated (SPS Spin150, SPS-international, The Netherlands) on a glass microscope slide (with thickness ~ 150 μm), and it was left to cure overnight at 65°C (Fig. 1(a)). The surfaces of the PDMS chip and the microscope slide were activated by exposing them to air plasma (50 W) for 40 s (Cute, Femto Science, South Korea), after which the microfluidic chip was bonded to the microscope slide, as displayed in Fig. 1(a). The activated chip was then used for cell seeding (Fig. 1(b)).

#### 2.1.2. Cell culturing and seeding

Human umbilical vein endothelial cells (HUVECs LO CC-2519, Westburg, The Netherlands) were cultured in pre-coated collagen culture flasks (#690950, Greiner Bio One2, The Netherlands) at 37°C and 5% $CO_2$ using endothelial cell growth medium 2 (EGM-2, #C-22111, PromoCell inc., Germany). Immediately after plasma activation, the chips were coated using a 0.1 mg/ml collagen solution (Collagen type-I, rat tail #A1048301, Thermofisher, The Netherlands). The coating was incubated at 37°C and 5% $CO_2$ for 1 hour. The coated chips were flushed with EGM-2 and prepared for cell seeding. HUVECs were removed from the cell culture flask by incubation with 3 ml Trypsin-EDTA (#15400054, Thermofisher, The Netherlands) for 3 minutes at 37°C and 5% $CO_2$. A cell culture medium in a 1 : 2 ratio was added to the flask to inactivate trypsin. The cells were centrifuged for 5 minutes at 390×g and counted using a brightfield cell counter (Lunatrade; automated cell counter, Logos Biosystems, France). The cells were seeded on the top and bottom of the channel at $15 \times 10^6$ cells/ml for at least 30 min for HUVECs to attach (Fig. 1(b)). A total of 150 μl of EGM-2 were added to the microfluidic channels, and the chips were placed on a rocking table (BenchBlottertrade; 2D platform rocker, Benchmark Scientific, USA) inside the incubator for 24 hours, after which a perfusable monolayer was formed (Fig. 1(b) and Fig. 1(d)). To observe the endothelial monolayer, F-actin and DNA in the cells were stained

Biomedical Optics EXPRESS

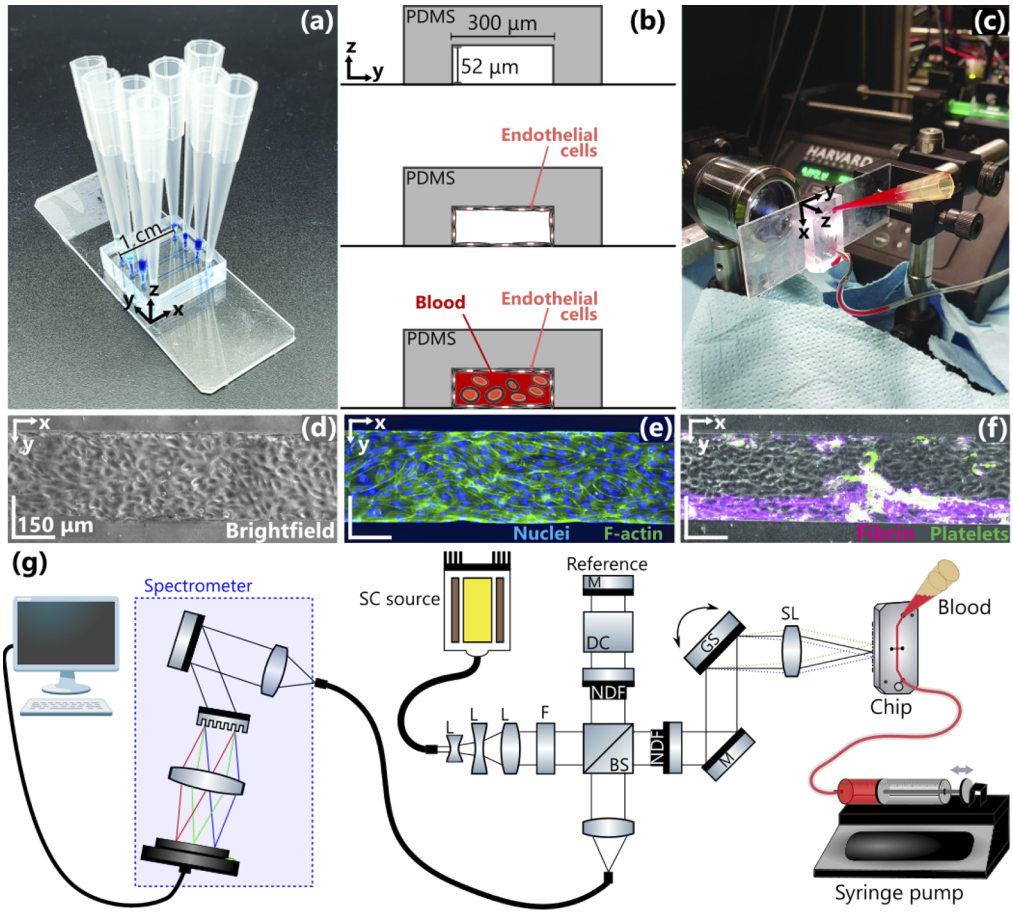


**Fig. 1.** Overview of blood perfusion assay using OCT imaging. **(a)** The microfluidic chip is made from PDMS and contains 4 straight channels assessable separately. **(b)** The microfluidic chip consists of a 1 cm long channel with 300 × 52 µm width and height. These channels are seeded with HUVECs and after 24 hours a monolayer has formed, then blood can be perfused through the channels. **(c)** Overview of blood perfusion set-up when imaging using OCT. **(d)** Brightfield image of the quiescent cell monolayer. **(e)** Fluorescent microscopy image of the monolayer distinguishing nuclei in blue and F-actin in green. **(f)** After the blood perfusion assay thrombus markers such as fibrin (in purple) and platelets (in green) are imaged using a fluorescent microscope. **(g)** Schematic illustration of the vis-OCT set-up used to monitor thrombus formation. L: lens, SC: supercontinuum source, F: low-pass filter, NDF: neutral density filter, BS: beam splitter, DC: dispersion compensation element, M: mirror, GS: galvanometer scanner, SL: scanning lens.

with Phalloidin-A488 and DAPI (R37110, R37605, Thermofisher, the Netherlands) as depicted in Fig. 1(e).

### 2.1.3. Blood perfusion assay

The Experimental Centre for Technical Medicine (ECTM, Techmed Centre, University of Twente) provided human whole blood samples. The local medical research ethics committee (METC Twente) approved the blood collection procedure. In agreement with the Declaration of Helsinki, all volunteers gave written informed consent. Whole blood samples were collected in vacuvette

Biomedical Optics EXPRESS

tubes containing 3.2% citrate (#455322, GreinerBio, The Netherlands). The samples were used within 4 hours after the blood draw. The first tube was discarded due to the risk of contamination with tissue thromboplastin during the blood draw [56]. Then, platelets and fibrin were stained with CD41-PE (1% (v/v), #MHCD4104, Thermo Fisher, The Netherlands) and fluorescein-conjugated fibrinogen (Fibrinogen from human plasma, #F13192, Invitrogen, The Netherlands) respectively for 10 minutes. A bent 14 gauge blunt needle replaced the outlet pipette tip and connected the chip through tubing (Tygon, Fishersci, The Netherlands) to a syringe pump (Harvard PHD 2000, Harvard Apparatus, USA). Immediately before the perfusion assay, blood was recalcified using a recalcification buffer containing HEPES (15630080, Thermofisher, The Netherlands), 63.2 mM $CaCl_2$ (1 M stock, #21115, Merck, Germany), and 31.6 mM $MgCl_2$ (#J61014.AK, Thermofisher, The Netherlands). During blood perfusion, the pump pulled blood through the channel at 7.8 µl/min for ~ 15 minutes, as shown in Fig. 1(c). After that, the channels were flushed with EGM-2 and fixated with 4% formaldehyde for 15 minutes. Finally, an EVOS M5000 imaging system (Thermo Fisher, The Netherlands) was used to obtain microscopy validation images at 4× magnification, as shown in Fig. 1(f).

## 2.2. Optical coherence tomography

### 2.2.1. OCT system

We use a custom-built OCT system optimized for visible light, described in detail in our previous work [27,57] and schematized in Fig. 1(g). Briefly, light propagates from a supercontinuum broadband source (SC, SuperK EXTREME EXB-6, NKT Photonics, Denmark) through three lenses (L1: LD2746-A, L2: LD2060-A, L3: LB1471-A, Thorlabs, USA) that expand and collimate the beam. A short-pass filter (FESH0700, Thorlabs, USA) filters out all wavelengths above 700 nm before the light arrives at the open-air Michelson interferometer. In the interferometer, a 10 : 90 beam splitter (BS028, Thorlabs, USA) reflects 90% of the incoming light towards the reference arm and transmits 10% towards the sample arm. In the reference arm, a variable neutral density filter (NDC-50C-2M-A, Thorlabs, USA) controls the intensity of light propagating through a dispersion compensation block composed by a microscope slide equal to the one on which PDMS was molded (Section 2.1.1) and a lens-equivalent dispersion compensation glass (LSM03DC-VIS, Thorlabs, USA). Then, the reference mirror (PF10-03-P01, Thorlabs, USA) reflects the beam to the beam splitter. In the sample arm, a variable neutral density filter (NDC-50C-2M-A, Thorlabs, USA) attenuates the light propagating to a galvanometer scanner (8320K, Cambridge Technology, USA) that steers the beam. After the scanner, a scanning lens (LSM03-VIS, Thorlabs, USA) with a 39 mm focal length focuses the beam at the channel of the VoC device. The $1/e^2$ diameter of the focused beam is ~ 12 µm. Note that the system images the VoC device from the bottom, where the microscope slide is located (Fig. 1(c)). Backscattered light from the VoC and light reflected at the reference arm combine at the beam splitter and is collected by a single-mode fiber (S405XP, Thorlabs, USA). The fiber guides the light into a custom-built spectrometer (HoloSpec f/1.8i, Kaiser Optical Systems, USA), where a grating disperses it on a line camera (Sprint spL4096-140km, Basler, Germany). The camera has an exposure time of 58 µs at a line rate of 16.7 kHz for a delivered power at the sample of ~ 5 mW. The spectrometer has a spectral resolution of 0.1 nm within 480 – 660 nm. The collected spectrum has a full width at half-maximum of ~ 75 nm centered at 555 nm, leading to a theoretical axial resolution of ~ 1.8 µm in air.

### 2.2.2. Imaging protocol

At the beginning of the blood perfusion assay, VoCs were placed in the OCT setup with the bottom of the microscope slide facing towards the system (Fig. 1(c)) and were imaged continuously for 15 minutes. The acquisition of one entire volume lasted ~30 s with a conventional raster scan pattern. A volume was composed of 156 B-scans separated ~ 4.5 µm (0.7 mm in total along

Biomedical Optics EXPRESS

the $y$-axis). Each B-scan ($zx$ plane) spanned $0.9 \times 2$ mm and consisted of $1024 \times 512$ pixels (in $z$ and $x$ respectively). Every A-line was repeated two times, before moving to the next $x$ location, to allow the calculation of the correlation between consecutive scans. After the blood assay and after flushing the VoC with EGM-2, an additional OCT scan of the flushed VoC was performed. During postprocessing, each OCT volume was flattened by aligning each A-line to the top boundary of the chip's channel.

#### 2.2.3. Correlation mapping

Correlation mapping is employed to distinguish between clotted regions and flowing blood. As demonstrated by Tang et al. [22], the autocorrelation of the OCT signal decreases as blood coagulates. We leverage this idea to create a spatial map of the correlation and determine the presence of a thrombus by analyzing the difference in the correlation signal between two consecutive scans. For this method, the intensity from the first scan $I_{t,A}$ is correlated to the intensity of the second scan $I_{t,B}$ at each spatial location $(z, x)$ and time $t$. By evaluating the correlation across an entire B-scan, a correlation map $C_t(z, x)$ is calculated as [22,58]

$$C_t(z,x) = \frac{\sum_{i=1}^{I}\sum_{j=1}^{J}\left(\left[I_{t,A}(z_i,x_j) - \overline{I_{t,A}}\right]\left[I_{t,B}(z_i,x_j) - \overline{I_{t,B}}\right]\right)}{\sqrt{\sum_{i=1}^{I}\sum_{j=1}^{J}\left[I_{t,A}(z_i,x_j) - \overline{I_{t,A}}\right]^2}\sqrt{\sum_{i=1}^{I}\sum_{j=1}^{J}\left[I_{t,B}(z_i,x_j) - \overline{I_{t,B}}\right]^2}}, \tag{1}$$

where $I \times J$ is a window for which the correlation is calculated around the central point $(z, x)$, $\overline{I_{t,A}} = \frac{1}{IJ}\sum_{i=1}^{I}\sum_{j=1}^{J} I_{t,A}(z_i, x_j)$ and $\overline{I_{t,B}} = \frac{1}{IJ}\sum_{i=1}^{I}\sum_{j=1}^{J} I_{t,B}(z_i, x_j)$ correspond to the mean intensity within the correlation window at location $(z, x)$ for the two B-scans.

The correlation window spans $5 \times 5$ pixels ($4.4 \times 19.5$ μm in $zx$) as this offered a reasonable trade-off between resolution and noise. The resulting correlation map ranges between $-1$ and 1, indicating weak and strong correlations, respectively. While low correlation values indicate red blood cells undergoing rapid motion, strong correlations represent static tissue or thrombi moving at a lower velocity [22]. Commonly, high correlation values $\geq 0.6$ have indicated static tissue that does not undergo any motion [58–60]. However, in the case of forming thrombi, they may present slow motion and weak diffusivity. Therefore, we defined a forming thrombus when the correlation remains $\geq 0.4$ in our correlation maps. The correlation was retrieved for every acquisition, yielding a three-dimensional correlation map. This map was transformed into two-dimensional *en-face* views ($xy$ plane) by averaging $C_t$ over the height of the VoC (50 μm in $z$, Fig. 1(b)). The *en-face* correlation maps were binarized by thresholding $C_t \geq 0.4$. The thresholded maps at each time interval were utilized to retrieve qualitative and quantitative information from the thrombi. The thrombus size, count, and area were calculated with the function *bwboundaries* from MATLAB (version 2022a), assuming that the total area of one $xy$ pixel is 17.5 $\mu m^2$.

## 3. Results

### 3.1. Correlation-based thrombus formation

First, we evaluated thrombi formation by analyzing the evolution of the correlation map as a function of time. Figure 2 shows the OCT intensity and correlation map during the blood perfusion assay. *En-face* and cross-sectional views of the OCT intensity from the VoC at the beginning of the assay are displayed in Fig. 2(a). From these cross-sectional views, it can be observed that the flowing blood produces a homogeneous intensity distribution inside the flow channel, while the boundary of the channel has higher intensity due to the presence of HUVECs and medium change. *En-face* images were produced by averaging the intensity in the red box in the cross-sections of Fig. 2 within the channel boundaries. The corresponding correlation map in

Biomedical Optics EXPRESS

Fig. 2(b) presents low correlation ($C_t \leq 0.4$), which indicates homogeneous flow. Small patches with high correlation $C_t \geq 0.4$ arise at the beginning of the assay, which are attributable to early thrombus formation. As time progresses, Fig. 2(c) exhibits low-intensity regions. These can be related to developing thrombi, where the accumulation of red blood cells attenuates more light than the free-flowing erythrocytes. The correlation map in Fig. 2(d) confirms the development and expansion of thrombi as the correlation value increases over time for the regions where lower flow is expected due to thrombus formation. The two spots indicated by the red arrows show the origin of two thrombi that become visible ~ 7 minutes into the assay. In their surrounding areas, the correlation is higher as time passes and the thrombus size increases. In contrast, the blue arrow indicates an area where homogeneous flow is present, and the correlation map has low variation compared to those where thrombi have formed.

### 3.2. Thrombus formation validation

After the blood perfusion assay, the flow channel was flushed with the cell culture medium and an additional OCT scan was performed. Figure 3(a) shows the OCT intensity of the flushed VoC, where the final thrombi are visible. The cross-sectional views reveal that thrombi occupy the full height of the channel. In Fig. 3(b), the last correlation map, just before flushing, displays a significant portion of the chip where the correlation is below the defined threshold $C_t \leq 0.4$.

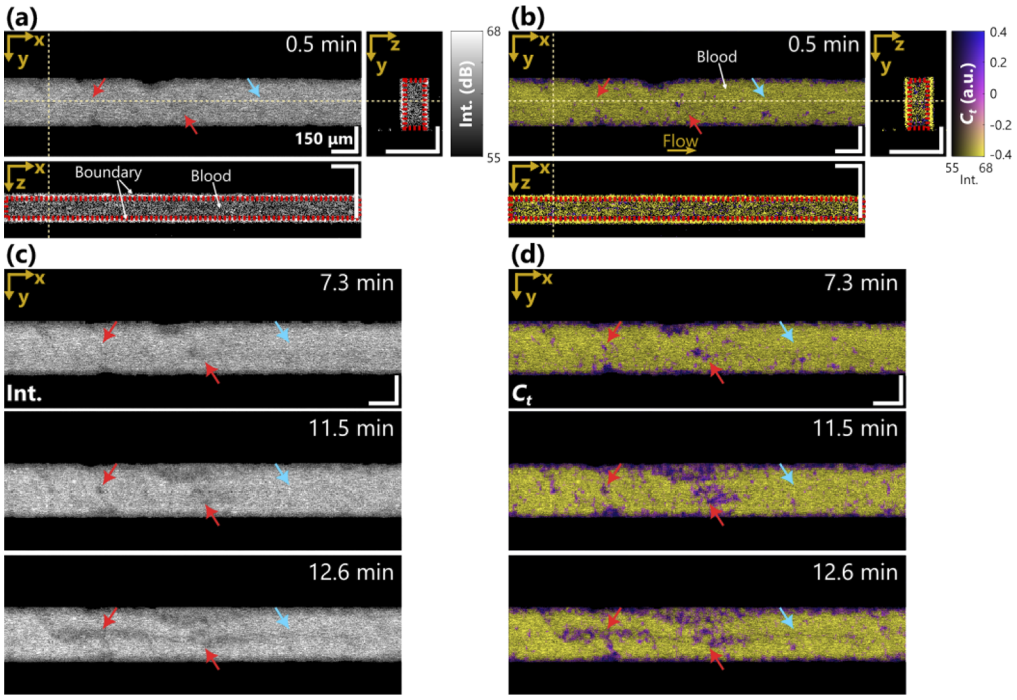


**Fig. 2.** OCT intensity and correlation at selected times during the blood perfusion essay. **(a)** *En-face* and cross-sectional views of the VoC with flowing blood at the beginning of the blood perfusion assay, the channel boundary is visible in the cross-sectional views. **(b)** *En-face* view and cross-sections of the correlation map $C_t$ overlaid with the intensity in **(a)** derived with Eq. (1) from **(a)**. *En-face* images in **(a)** and **(b)** were produced by averaging the values within the red box indicated in the cross-sections. **(c)** *En-face* intensity and **(d)** correlation as a function of time during the blood perfusion assay. Red arrows indicate the origin of a thrombus. The blue arrow indicates a region without clotting. A video of the entire perfusion assay can be found in Visualization 1.

Biomedical Optics EXPRESS

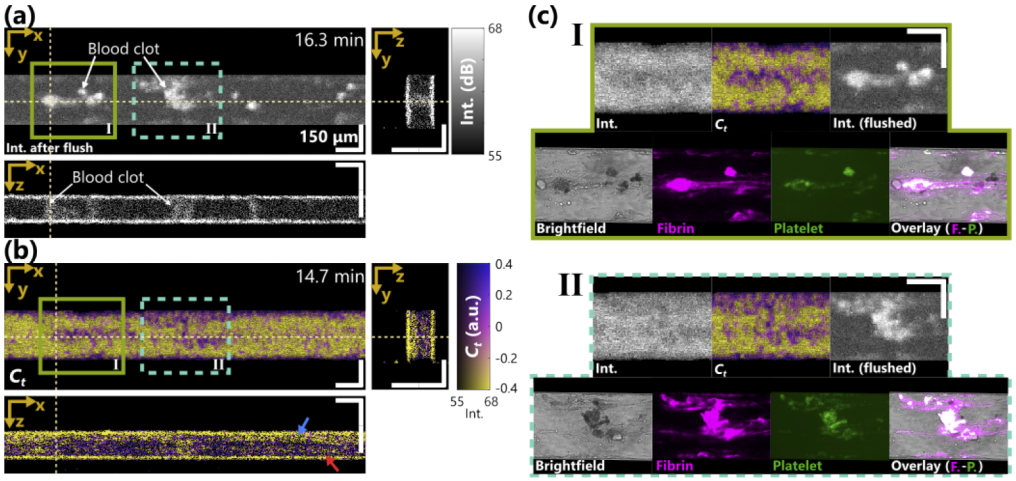


**Fig. 3.** Thrombus formation and validation with microscopy images. **(a)** OCT intensity of the VoC after flushing. **(b)** Last correlation map before flushing the VoC, exhibiting the presence of thrombi. The red arrow indicates a clotted region inside the channel. As pointed out by the blue arrow, thrombi do not occupy the entire height of the channel, allowing blood to flow in the upper part of the channel. **(c)** OCT images from the regions of interest **I** and **II** in **(a)** and **(b)**, and respective comparison with images obtained in the microscope consisting of brightfield, fibrin and platelets markers, and the corresponding overlay.

Although some thrombi in the correlation map nearly occupy the entire height of the channel (red arrow, Fig. 3(b)), the presence of blood flow (blue arrow, Fig. 3(b)) was maintained and observed throughout the entire experiment. *En-face* images in Fig. 3(a) and 3(b) reveal a similar location where thrombi are expected from the correlation and are visible after flushing. The slight shift in the *x*-axis in Fig. 3(a) is due to the minor movement of the chip after the tip with blood (Fig. 1(b)) was removed.

Figure 3(c) shows a direct comparison between the OCT signal and microscopy images taken after the blood perfusion assay at two different locations in the microfluidic channel, indicated by box **I** (solid green line) and **II** (dashed blue line) in Fig. 3(a) and 3(b). During the blood perfusion assay, the thrombi produce lower intensity and high correlation. In contrast, after flushing, thrombi display higher intensity since scattering arises only at these locations. Because the blood was pre-stained with the fluorescent markers for fibrin (purple) and platelets (green), thrombi were imaged after the blood perfusion assay. The first and second rows of the regions of interest **I** and **II** in Fig. 3(c) show a similar shape and size among the correlation map, the OCT flushed signal and the microscopy images. The overlay image shows activated platelet adherence and fibrin threads at the site of the suspected thrombi. A visual comparison between the brightfield image and the flushed OCT channel reveals a similar pattern, differentiated by the lower resolution of OCT compared to the microscope.

### 3.3. *Thrombus growth*

Finally, we evaluated the development of the thrombi and the total clotted area over time. Figure 4 presents the evolution of the thrombus formation in the channel over time. After thresholding the correlation maps, a specific color was assigned for a given time, assigning the correlation as a clotting marker over time. Figure 4(a) is the color-encoded representation of the correlation marker during the perfusion assay. At the beginning of the assay, the boundaries of the channel have small thrombi that remain attached to it until the end of the process. The initial thrombi are

Biomedical Optics EXPRESS

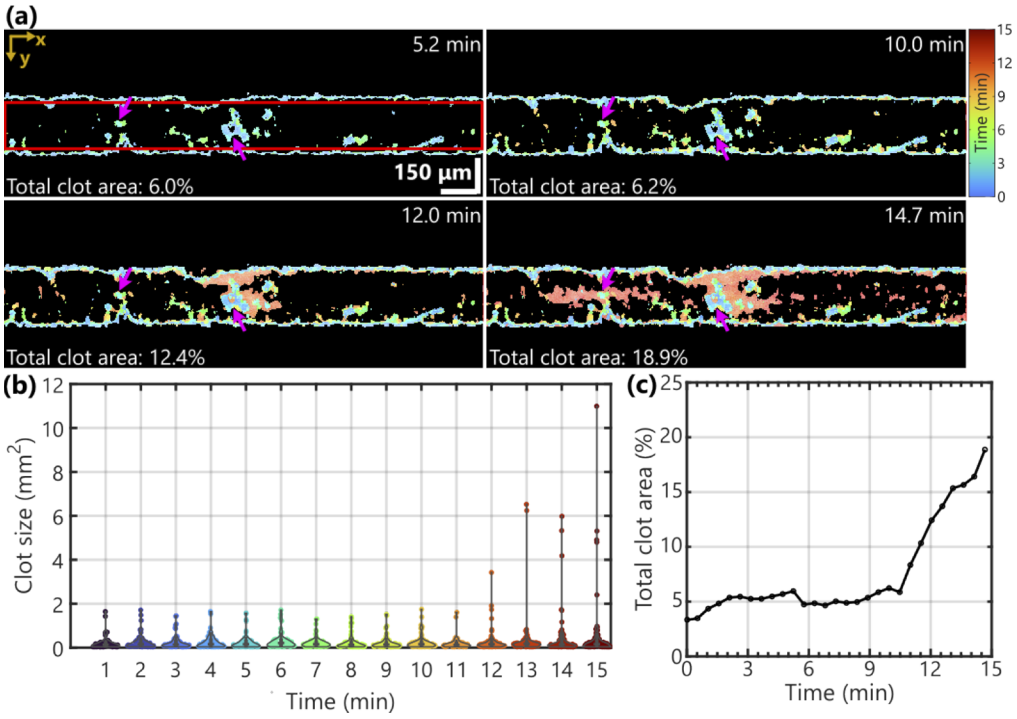


**Fig. 4.** Thrombus growth and evolution over time. **(a)** Color-coded location of clotted blood over time. The color represents the time at which a $C_t \geq 0.4$ was registered. The clotted area increases over time as the assay progresses. The purple arrows indicate the presumed origin of two thrombi. **(b)** Violin plot showing the distribution of thrombi over time within the red box in **(a)** (excluding the flow channel boundaries). As the assay progresses, bigger clots appear as red blood cell aggregates grow. **(c)** Total percentage area of the channel with thrombi as a function of time. A video of the thrombus growth can be found in Visualization 2.

visible short into the assay (~ 5 min) and highlighted with purple arrows in Fig. 4(a). After ~ 10 min, the thrombi have minimally expanded, and the channel allows free blood flow. After ~ 12 min, the thrombus indicated by the right purple arrow has grown significantly and continues to expand until the end of the assay (~ 15 min). By the end of the assay, a large thrombus forms around the left purple arrow, and smaller thrombi emerge through the channel.

Figure 4(b) summarizes the dynamic behavior of thrombi formation. The violin plot (obtained from the area inside the red box in Fig. 4(a)) shows that for the majority of the process (~ 11 min), the thrombus count and size remain constant. However, at the later stages of the process, bigger thrombi emerge and expand. Figure 4(c) demonstrates that the total area covered by thrombi inside the flow channel increases over time as a percentage of the flowing area.

## 4. Discussion

In this work, we demonstrated that OCT can visualize the spatial and temporal changes during thrombi formation without fluorescent markers in flowing blood. A microfluidic VoC device mimicked the interaction between human-whole blood and endothelial cells, enabling localization of the thrombi. The VoC combined with a vis-OCT system allowed simulation and imaging of thrombi formation based on the correlation of the OCT signal. With the correlation between two consecutive B-scans, we observed thrombi formation by thresholding the increase in correlation

Biomedical Optics EXPRESS

due to reduced blood flow during thrombus formation. Our observations were validated with fluorescence microscopy images highlighting fibrin and platelets as thrombus markers. The correlation map at the end of the perfusion assay, the intensity after flushing the VoC channel, and the microscopy images showed similarities in location, size, and geometry. Finally, we quantified thrombus formation by measuring the thrombus size and chip thrombus-covered area as a function of time. In the remaining discussion, we review relevant aspects of our results.

### 4.1. Thrombus formation monitoring

From the OCT data, we could detect thrombi formation in the VoC. As presented in Fig. 2, the OCT signal shows thrombi as a lower-intensity signal, indicating more scattering and absorption by red blood cells. The presence of thrombi is even more notorious when analyzing the correlation signal. We found that if the size of the high correlation area increases over time (as presented in Fig. 4), those spots mark the origin of the thrombi. However, we recognized that the constant blood flow washed out some of the thrombi from the field of view. We attribute this behavior to forming thrombi lacking adherence to the cell layer. The $zx$ cross-section in Fig. 3(a) shows that the thrombi seem connected to the upper and bottom cell layers, but some thrombi do not cover the extent of the chip. This unattached thrombus could not be observed during the blood perfusion assay, due to the constant change in correlation produced by the blood flow, as shown in the $zx$ cross-section in Fig. 3(b). Another limitation of the vis-OCT system that was employed in this study is the low acquisition rate compared to wavelength-swept source OCT (SS-OCT) systems [61,62]. Increasing the sampling rate could reveal thrombus expansion in three dimensions. However, the availability of SS-OCT systems in the visible wavelength range is limited, and higher resolution (in the order of 5 μm) is beneficial to observe thrombus formation [63].

### 4.2. Correlation mapping as thrombus marker

We noticed that the global correlation of the OCT signal increases over time during the blood perfusion assay. We attribute this behavior to the overall change in the viscoelastic properties of the blood and the expected coagulation over the assay duration [22]. In the flowing blood, thrombi attached to endothelial cells do not undergo the rapid motion of the free-flowing red blood cells, thus increasing the local correlation when compared to the rapid change experienced by moving red blood cells. Therefore, we defined a thrombus as a region where the correlation $C_t \geq 0.4$ in the flowing blood. The correlation threshold for forming thrombi can vary among OCT systems since the correlation depends on the camera line rate, the spatial sampling, and the number of B-scans averaged [58,59]. Additionally, multiple scattering has been shown to affect the decorrelation rate of flowing whole-blood [64]. In our model, we have assumed single scattering behavior inside the relatively small height of the channel (50 μm) and we assumed that the rate of decorrelation induced by multiple scattering is below the defined threshold. However, multiple scattering effects by blood may contribute to image blurring of the thrombi in the correlation maps, compared to the intensity images of the flushed channels (Fig. 3(a)). A limitation of the method is that we do not measure platelets or fibrin aggregation directly, but rather the changes in flow, which could lead to false positives in the data. A shadow effect can be presented in front of the thrombus in the propagation axis of the beam due to a limited flow which is not due to an aggregate itself [59]. However, looking at the data after flushing, we have captured the final thrombus reasonably well. The shadow effect is negligible for endpoint measurements.

### 4.3. Validation with microscopy

As presented in Fig. 3(a) and Fig. 3(b), visual inspection of the blood clots show a correspondence in location, shape, and size. However, due to the intermediate flushing step, the exact size and shape of the thrombi before flushing is unknown. Therefore, our correlation-based estimation of

Biomedical Optics EXPRESS

the thrombus size and area may be biased compared to the actual thrombus size after flushing. Figure 3(c) exhibits the limitation of conventional OCT intensity to identify blood clots since the contrast is low compared to the flowing blood. The brightfield image and fibrin and platelet markers in Fig. 3(c) have a similar appearance to the intensity of the flushed chip in OCT, even though OCT has a lower resolution. These images reveal a high correspondence between $C_t$ at the end of the process and the location of the blood clots.

### 4.4. Blood-vessel on a chip device

The VoC was based on microchannels with rectangular geometries, these channels are 300 μm wide and 50 μm high, which does not represent the human artery with respect to size as well as shape. The size of human arteries can range from 25 to 60 mm. To overcome the differences in size, the flow rate was meticulously chosen to mimic an arterial shear rate of 1000 $s^{-1}$. The rectangular shape of these VoCs is an abstraction of the actual anatomy of blood vessels *in vivo*. In the VoC, flowing blood components will experience a lower forward velocity at the boundary of the rectangular geometry compared to a circular channel, leading to higher residence time and exacerbated fibrin deposition. Consequently, we excluded the boundary areas from the analyses of thrombus formation (outside the red box in Fig. 4(a)), as described previously [37], these areas induce artifacts that can affect the data analysis. Cylindrical VoC models [65–67] could be used to mimic the *in vivo* geometry more closely. The height of these cylindrical models is $\sim 250 - 300$ μm and OCT could unveil the interaction between endothelial cells and flowing blood in arterioles and venules. In our study, HUVECs were used to line the VoC. Although they are a commonly used cell type in blood vessel modeling, these cells can only be obtained from newborns, and not from specific patients, thereby limiting the applicability of the VoC in disease modeling. Therefore, similar research on using OCT to analyze blood clotting in VoCs with human induced pluripotent stem cells-derived endothelial cells (hiPSC-ECs) could determine patient-specific clotting mechanisms and responses.

## 5. Conclusion

In conclusion, we have used vis-OCT to monitor the spatial and temporal changes in the formation of thrombi in a VoC device. The VoC containing HUVECs simulated the interaction between flowing blood and endothelial cells. The OCT correlation signal provided a marker to observe the evolution of thrombi over time. By thresholding the correlation, we tracked the origin and growth of thrombi. The thrombi detected from the correlation signal were similar in shape and size when comparing the OCT intensity measurements after flushing the chip and the microscopy images. Those microscopy images validated the presence of thrombi. As this pattern is also present in the correlation map, our results suggest the possibility of live image thrombus formation without the necessity of fluorescent markers. Furthermore, we were able to visualize the thrombus formation in width and length and provide a framework for further analysis in height. This dimension could not be determined in real-time using previous fluorescent marker experiments, but only as an end-point measurement using confocal microscopy. Thus, we show a new non-invasive technique to measure thrombus formation in real-time in three dimensions. This technique can now be applied in different, more complex, VoC systems to obtain a greater understanding of thrombus formation and development and with that personalized drug development.

**Funding.** Netherlands Organ-on-Chip Initiative (024.003.001).

**Acknowledgments.** The authors acknowledge the assistance from the Experimental Centre for Technical Medicine with the blood collection process.

**Disclosures.** The authors declare no conflicts of interest related to this work.

**Data availability.** The data sets and algorithms generated and analyzed for this manuscript are available by contacting the corresponding authors upon reasonable request.

Biomedical Optics EXPRESS

## References


1. S. Palta, R. Saroa, and A. Palta, "Overview of the coagulation system," Indian J. of Anaesth. **58**(5), 515–523 (2014).
2. M. H. Periayah, A. S. Halim, and A. Z. M. Saad, "Mechanism action of platelets and crucial blood coagulation pathways in hemostasis," Int. J. Hematol. Oncol. Stem Cell Res. **11**, 319–327 (2017).
3. J. Stone, P. Hangge, H. Albadawi, A. Wallace, F. Shamoun, M. G. Knuttien, S. Naidu, and R. Oklu, "Deep vein thrombosis: pathogenesis, diagnosis, diagnosis, and medical management," Cardiovasc. Diagn. and Ther. **7**(S3), S276–S284 (2017).
4. D. A. Anaya and A. B. Nathens, "Thrombosis and coagulation: Deep vein thrombosis and pulmonary embolism prophylaxis," Surg. Clin. North Am. **85**(6), 1163–1177 (2005).
5. M. Hepburn-Brown, J. Darvall, and G. Hammerschlag, "Acute pulmonary embolism: a concise review of diagnosis and management," Internal Medicine Journal **49**(1), 15–27 (2019).
6. C. J. Sommer, "Ischemic stroke: experimental models and reality," Acta Neuropathol. **133**(2), 245–261 (2017).
7. S. K. Feske, "Ischemic stroke," The Am. J. Med. **134**(12), 1457–1464 (2021).
8. A. Siniarski, A. Gasecka, J. A. Borovac, P. E. Papakonstantinou, D. Bongiovanni, H. Ehrlinder, M. Giustozzi, R. A. Guerreiro, and W. A. E. Parker, "Blood coagulation disorders in heart failure: from basic science to clinical perspectives," J. Card. Fail. **29**(4), 517–526 (2023).
9. L. Lu, M. Liu, R. Sun, Y. Zheng, and P. Zhang, "Myocardial infarction: symptoms and treatments," Cell Biochem. Biophys. **72**(3), 865–867 (2015).
10. M. M. Aria, A. Erten, and O. Yalcin, "Technology advancements in blood coagulation measurements for point-of-care diagnostic testing," Front. Bioeng. Biotechnol. **7**, 395 (2019).
11. B. Ramaswamy, Y.-T. T. Yeh, and S.-Y. Zheng, "Microfluidic device and system for point-of-care blood coagulation measurement based on electrical impedance sensing," Sens. Actuators, B **180**, 21–27 (2013).
12. H. Berney and J. J. O'Riordan, "Impedance measurement monitors blood coagulation," Anal. Dialogue **42**, 08 (2008).
13. K. F. Lei, K.-H. Chen, P. Tsui, and N.-M. Tsang, "Real-time electrical impedimetric monitoring of blood coagulation process under temperature and hematocrit variations conducted in a microfluidic chip," PLoS One **8**(10), e76243 (2013).
14. M. Liu, K. Zaman, and Y. M. Fortenberry, "Overview of the therapeutic potential of aptamers targeting coagulation factors," Int. J. Mol. Sci. **22**(8), 3897 (2021).
15. D. Chen, S. Song, J. Ma, Z. Zhang, P. Wang, W. Liu, and Q. Guo, "Micro-electromechanical film bulk acoustic sensor for plasma and whole blood coagulation monitoring," Biosens. Bioelectron. **91**, 465–471 (2017).
16. O. Cakmak, E. Ermek, N. Kilinc, S. Bulut, I. Baris, I. H. Kavakli, G. G. Yaralioglu, and H. Urey, "A cartridge based sensor array platform for multiple coagulation measurements from plasma," Lab Chip **15**(1), 113–120 (2015).
17. Z. Chen, J. Lu, C. Zhang, I. Hsia, X. Yu, L. Marecki, E. Marecki, M. Asmani, S. Jain, S. Neelamegham, and R. Zhao, "Microclot array elastometry for integrated measurement of thrombus formation and clot biomechanics under fluid shear," Nat. Commun. **10**(1), 2051 (2019).
18. A. B. Karpiouk, S. R. Aglyamov, S. Mallidi, J. Shah, W. G. Scott, J. M. Rubin, and S. Y. Emelianov, "Combined ultrasound and photoacoustic imaging to detect and stage deep vein thrombosis: phantom and *ex vivo* studies," J. Biomed. Opt. **13**(5), 054061 (2008).
19. M. A. Juratli, Y. A. Menyaev, M. Sarimollaoglu, A. V. Melerzanov, D. A. Nedosekin, W. C. Culp, J. Y. Suen, E. I. Galanzha, and V. P. Zharov, "Noninvasive label-free detection of circulating white and red blood clots in deep vessels with a focused photoacoustic probe," Biomed. Opt. Express **9**(11), 5667–5677 (2018).
20. X. Xu, J. Lin, and F. Fu, "Optical coherence tomography to investigate optical properties of blood during coagulation," J. Biomed. Opt. **16**(9), 096002 (2011).
21. X. Xu, J. Zhu, and Z. Chen, "Dynamic and quantitative assessment of blood coagulation using optical coherence elastography," Sci. Rep. **6**(1), 24294 (2016).
22. Y. Tang, J. Zhu, L. Zhu, F. Fan, Z. Ma, and F. Zhang, "Blood coagulation monitoring under static and flow conditions with optical coherence tomography autocorrelation analysis," Appl. Phys. Lett. **120**(16), 163702 (2022).
23. X. Xu, J. Geng, and X. Teng, "Monitoring the blood coagulation process under various flow conditions with optical coherence tomography," J. Biomed. Opt. **19**(4), 046021 (2014).
24. S. P. Chong, C. W. Merkle, C. Leahy, H. Radhakrishnan, and V. J. Srinivasan, "Quantitative microvascular hemoglobin mapping using visible light spectroscopic optical coherence tomography," Biomed. Opt. Express **6**(4), 1429–1450 (2015).
25. S. Pi, T. T. Hormel, X. Wei, W. Cepurna, B. Wang, J. C. Morrison, and Y. Jia, "Retinal capillary oximetry with visible light optical coherence tomography," Proc. Natl. Acad. Sci. U. S. A. **117**(21), 11658–11666 (2020).
26. X. Xu and X. Teng, "Effect of fibrinogen on blood coagulation detected by optical coherence tomography," Phys. Med. Biol. **60**(10), 4185–4195 (2015).
27. C. Cuartas-Vélez, C. Veenstra, S. Kruitwagen, W. Petersen, and N. Bosschaart, "Optical density based quantification of total haemoglobin concentrations with spectroscopic optical coherence tomography," Sci. Rep. **11**(1), 8680 (2021).
28. W. Drexler and J. G. Fujimoto, *Optical coherence tomography: Technology and applications* (Springer Reference, 2015).
29. B. R. Branchford, C. J. Ng, K. B. Neeves, and J. D. Paola, "Microfluidic technology as an emerging clinical tool to evaluate thrombosis and hemostasis," Thromb. Res. **136**(1), 13–19 (2015).

Biomedical Optics EXPRESS


30. J. Cable, P. Arlotta, and K. K. Parker, *et al.*, "Engineering multicellular living systems–a keystone symposia report," Ann. N. Y. Acad. Sci. **1518**(1), 183–195 (2022).
31. E. Ko and R. D. Kamm, "Neurovascular models for organ-on-a-chips," Vitr. Model. **1**(2), 125–127 (2022).
32. D. R. Myers and W. A. Lam, "Vascularized microfluidics and their untapped potential for discovery in diseases of the microvasculature," Annu. Rev. Biomed. Eng. **23**(1), 407–432 (2021).
33. J. Ko, D. Park, S. Lee, B. Gumuscu, and N. L. Jeon, "Engineering organ-on-a-chip to accelerate translational research," Micromachines **13**(8), 1200 (2022).
34. V. Paloschi, M. Sabater-Lleal, H. Middelkamp, A. Vivas, S. Johansson, A. van der Meer, M. Tenje, and L. Maegdefessel, "Organ-on-a-chip technology: a novel approach to investigate cardiovascular diseases," Cardiovasc. Res. **117**(14), 2742–2754 (2021).
35. N. K. R. Pandian, R. G. Mannino, W. A. Lam, and A. Jain, "Thrombosis-on-a-chip: Prospective impact of microphysiological models of vascular thrombosis," Curr. Opin. Biomed. Eng. **5**, 29–34 (2018).
36. H.-H. G. Song, R. T. Rumma, C. K. Ozaki, E. R. Edelman, and C. S. Chen, "Vascular tissue engineering: progress, challenges, and clinical promise," Cell Stem Cell **22**(3), 340–354 (2018).
37. H. J. Albers, R. Passier, A. van den Berg, and A. D. van der Meer, "Automated analysis of platelet aggregation on cultured endothelium in a microfluidic chip perfused with human whole blood," Micromachines **10**(11), 781 (2019).
38. P. F. Costa, H. J. Albers, J. E. A. Linssen, H. H. T. Middelkamp, L. van der Hout, R. Passier, A. van den Berg, J. Malda, and A. D. van der Meer, "Mimicking arterial thrombosis in a 3d-printed microfluidic: In vitro vascular model based on computed tomography angiography data," Lab Chip **17**(16), 2785–2792 (2017).
39. A. Hasan, A. Paul, A. Memic, and A. Khademhosseini, "A multilayered microfluidic blood vessel-like structure," Biomed. Microdevices **17**(5), 88 (2015).
40. L. Jia, F. Han, H. Yang, G. Turnbull, J. Wang, J. Clarke, W. Shu, M. Guo, and B. Li, "Microfluidic fabrication of biomimetic helical hydrogel microfibers for blood-vessel-on-a-chip applications," Adv. Healthcare Mater. **8**(13), 1900435 (2019).
41. R. G. Mannino, D. R. Myers, B. Ahn, Y. Wang, M. Rollins, H. Gole, A. S. Lin, R. E. Guldberg, D. P. Giddens, L. H. Timmins, and W. A. Lam, "Do-it-yourself in vitro vasculature that recapitulates in vivo geometries for investigating endothelial-blood cell interactions," Sci. Rep. **5**(1), 12401 (2015).
42. M. Tsai, A. Kita, J. Leach, R. Rounsevell, J. N. Huang, J. Moake, R. E. Ware, D. A. Fletcher, and W. A. Lam, "In vitro modeling of the microvascular occlusion and thrombosis that occur in hematologic diseases using microfluidic technology," J. Clin. Invest. **122**(1), 408–418 (2012).
43. C. G. M. van Dijk, M. M. Brandt, N. Poulis, J. Anten, M. van der Moolen, L. Kramer, E. F. G. A. Homburg, L. Louzano-Martinez, J. Pei, M. M. Krebber, B. W. M. van Balkom, P. de Graaf, D. J. Duncker, M. C. Verhaar, R. Luttge, and C. Cheng, "A new microfluidic model that allows monitoring of complex vascular structures and cell interactions in a 3d biological matrix," Lab Chip **20**(10), 1827–1844 (2020).
44. E. Westein, A. D. van der Meer, M. J. E. Kuijpers, J.-P. Frimat, A. van den Berg, and J. W. M. Heemskerk, "Atherosclerotic geometries exacerbate pathological thrombus formation poststenosis in a von willebrand factor-dependent manner," Proc. Natl. Acad. Sci. U. S. A. **110**(4), 1357–1362 (2013).
45. Y. Zheng, J. Chen, M. Craven, N. W. Choi, S. Totorica, A. Diaz-Santana, P. Kermani, B. Hempstead, C. Fischbach-Teschl, J. A. López, and A. D. Stroock, "In vitro microvessels for the study of angiogenesis and thrombosis," Proc. Natl. Acad. Sci. U. S. A. **109**(24), 9342–9347 (2012).
46. S. Cai, H. Li, F. Zheng, F. Kong, M. Dao, G. E. Karniadakis, and S. Suresh, "Artificial intelligence velocimetry and microaneurysm-on-a-chip for three-dimensional analysis of blood flow in physiology and disease," Proc. Natl. Acad. Sci. U. S. A. **118**(13), e2100697118 (2021).
47. P. Elizondo and A. L. Fogelson, "A mathematical model of venous thrombosis initiation," Biophys. J. **111**(12), 2722–2734 (2016).
48. Y. C. Zhao, P. Vatankhah, T. Goh, R. Michelis, K. Kyanian, Y. Zhang, Z. Li, and L. A. Ju, "Hemodynamic analysis for stenosis microfluidic model of thrombosis with refined computational fluid dynamics simulation," Sci. Rep. **11**(1), 6875 (2021).
49. P. Balogh and P. Bagchi, "A computational approach to modeling cellular-scale blood flow in complex geometry," J. Comput. Phys. **334**, 280–307 (2017).
50. R. Wagenvoord, P. W. Hemker, and H. C. Hemker, "The limits of simulation of the clotting system," J. Thromb. Haemost. **4**(6), 1331–1338 (2006).
51. Y. Chen and L. Ju, "Biomechanical thrombosis: The dark side of force and dawn of mechano-medicine," Stroke Vasc. Neurol. **5**(2), 185–197 (2020).
52. S. P. Jackson, W. S. Nesbitt, and E. Westein, "Dynamics of platelet thrombus formation," J. Thromb. Haemost. **7**, 17–20 (2009).
53. A. Rana, E. Westein, B. Niego, and C. E. Hagemeyer, "Shear-dependent platelet aggregation: mechanisms and therapeutic opportunities," Front. Cardiovasc. Med. **6**, 141 (2019).
54. J. W. Yau, H. Teoh, and S. Verma, "Endothelial cell control of thrombosis," BMC Cardiovasc. Disord. **15**(1), 130 (2015).
55. Y. B. Arik, W. Buijsman, J. Loessberg-Zahl, C. Cuartas-Vélez, C. Veenstra, S. Logtenberg, A. M. Grobbink, P. Bergveld, G. Gagliardi, A. I. den Hollander, N. Bosschaart, A. van den Berg, R. Passier, and A. D. van der Meer,

Biomedical Optics EXPRESS

"Microfluidic organ-on-a-chip model of the outer blood-retinal barrier with clinically relevant read-outs for tissue permeability and vascular structure," Lab Chip **21**(2), 272–283 (2021).
56. N. Tekkeşin, O. B. Esen, C. Kilinç, and O. Eviyao glu, "Discard first tube for coagulation testing," Blood Coagul. Fibrinolysis **23**(4), 299–303 (2012).
57. C. Veenstra, W. Petersen, I. M. Vellekoop, W. Steenbergen, and N. Bosschaart, "Spatially confined quantification of bilirubin concentrations by spectroscopic visible-light optical coherence tomography," Biomed. Opt. Express **9**(8), 3581–3589 (2018).
58. A. Zhang, Q. Zhang, C.-L. Chen, and R. K. Wang, "Methods and algorithms for optical coherence tomography-based angiography: a review and comparison," J. Biomed. Opt. **20**(10), 100901 (2015).
59. J. Enfield, E. Jonathan, and M. Leahy, "*In vivo* imaging of the microcirculation of the volar forearm using correlation mapping optical coherence tomography (cmoct)," Biomed. Opt. Express **2**(5), 1184–1193 (2011).
60. W. J. Choi, R. Reif, S. Yousefi, and R. K. Wang, "Improved microcirculation imaging of human skin *in vivo* using optical microangiography with a correlation mapping mask," J. Biomed. Opt. **19**(3), 036010 (2014).
61. S. Chen, B. Potsaid, Y. Li, J. Lin, Y. Hwang, E. M. Moult, J. Zhang, D. Huang, and J. G. Fujimoto, "High speed, long range, deep penetration swept source oct for structural and angiographic imaging of the anterior eye," Sci. Rep. **12**(1), 992 (2022).
62. F. L. D. Huang, Z. He, Z. Cheng, C. Shang, and P. K. A. Wai, "400 mhz ultrafast optical coherence tomography," Opt. Lett. **45**(24), 6675–6678 (2020).
63. J. P. Kolb, T. Pfeiffer, M. Eibl, H. Hakert, and R. Huber, "High-resolution retinal swept source optical coherence tomography with an ultra-wideband fourier-domain mode-locked laser at mhz a-scan rates," Biomed. Opt. Express **9**(1), 120–130 (2018).
64. N. G. Ferris, T. M. Cannon, M. Villiger, B. E. Bouma, and N. Uribe-Patarroyo, "Forward multiple scattering dominates speckle decorrelation in whole-blood flowmetry using optical coherence tomography," Biomed. Opt. Express **11**(4), 1947–1966 (2020).
65. L. L. Bischel, S.-H. Lee, and D. J. Beebe, "A practical method for patterning lumens through ecm hydrogels via viscous finger patterning," J. Lab. Autom. **17**(2), 96–103 (2012).
66. A. Herland, A. D. van der Meer, E. A. FitzGerald, T.-E. Park, J. F. Sleeboom, and D. E. Ingber, "Distinct contributions of astrocytes and pericytes to neuroinflammation identified in a 3d human blood-brain barrier on a chip," PLoS One **11**(3), e0150360 (2016).
67. M. N. S. de Graaf, A. Cochrane, F. E. van den Hil, W. Buijsman, A. D. van der Meer, A. van den Berg, C. L. Mummery, and V. V. Orlova, "Scalable microphysiological system to model three-dimensional blood vessels," APL Bioeng. **3**(2), 026105 (2019).